Analysis of milling of dry compacted ribbons by distinct element method

C. Hare [a,*], M. Ghadiri [a], N. Guillard [b], T. Bosworth [b,c], G. Egan [b,c]

[a] Institute of Particle Science and Engineering, University of Leeds, Leeds LS2 9JT, UK
[b] Procter & Gamble, Newcastle Innovation Centre, Newcastle upon Tyne NE12 9BZ, UK
[c] Procter & Gamble, Bethel Technical Center, Bethel, CT, USA

HIGHLIGHTS

- Dry compacted ribbons were represented in DEM by bonded spheres.
- The bond strength was calibrated by experimental and simulated 3 point bend tests.
- DEM estimates impact velocities and stresses the ribbons experience in the mill.
- Ribbons are exposed to such impacts and stresses to predict size distribution.
- Predicted size distribution correlates well with plant data.

GRAPHICAL ABSTRACT
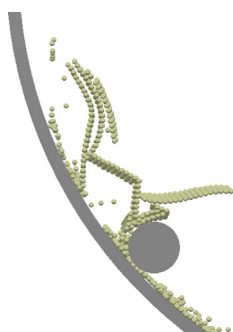
ARTICLE INFO

ABSTRACT

Fine cohesive powders are often dry granulated to improve their flowability. Roller compaction is commonly used to produce dense ribbons which are then milled. The material properties of the powder and the conditions in the roller compactor affect the strength of the ribbons, however there is no method in the literature to predict the size distribution of the product of ribbon milling. Here we introduce a method, by using the Distinct Element Method (DEM) to determine the prevailing impact velocities and stresses in the mill, with bonded spheres representing the ribbons. The bond strength is calibrated by matching experimental results of three point bend measurements and predictions from numerical simulations. The ribbons are then exposed to the dynamic conditions predicted by the DEM, by dropping them from a controlled height to cause fragmentation, and subsequently stressing them in a shear cell under the conditions again predicted by the DEM. The fragments are sheared under these conditions to represent repeated passage of bars over the fragments at the mill base. Sieve analysis is used here to determine the particle size distribution under given mill conditions. The predicted size distribution of the mill product compares well with the plant data. It is found that the mill speed and length of ribbons fed to the mill have no significant influence on the product size distribution for the range tested.

1. Introduction

Fine particulate materials often pose handling problems, such as poor flowability, adversely affecting dose uniformity. To overcome this, particle size can be increased by a variety of granulation methods, such as wet granulation in rotating or tumbling vessels

* Corresponding author.
E-mail address: c.hare@surrey.ac.uk (C. Hare).

(Salman et al., 2007), or dry granulation through direct compression in a roller compactor (Guigon et al., 2007), followed by milling. The products of a roller compactor are typically relatively large sheets, known as a ribbons (> 10 mm in length and width), and as such they are subjected to a subsequent size reduction process by milling. Miguelez-Moran et al. (2008) investigated the effect of lubricants on ribbon density and found that the method of loading in the compactor is crucial in determining density homogeneity, with average density increasing with peak pressure and nip angle. Khorasani et al. (2015) determined ribbon porosity using NIR, mercury porosimetry and oil intrusion, all of which indicated reduced ribbon porosity with compaction pressure. Muliadi et al. (2013) showed that the predicted density distribution of roller compacted pharmaceutical powders by Finite Element Method (FEM) can correlate well with experimentally-measured values by X-Ray Tomography (XRT). Both experiments and the FEM showed that when the rollers are free to move laterally the inlet stress does not affect the average ribbon density. Ribbon density and strength increase as the hardness of the feed material is reduced, as indicated by nano-indentation measurements (Al-Asady et al., 2015).

During milling the size reduction can be driven by impact, shear and compression to varying degrees, depending on the mill type, operational conditions and material properties. Consequently, it is difficult to determine the suitable conditions to use for milling of a given ribbon product from roller compaction. Vanarase et al. (2015) compared the performance of a hammer mill and a co-mill in milling extrudates of alumina-magnesia. It was shown that the impeller speed was influential in the size reduction in the co-mill, but not in the hammer mill. An increase in outlet mesh size leads to a coarser product, with the hammer mill being more efficient in allowing particles closer to the mesh size to exit. Samata et al. (2012) showed that the profile of the screen in a cone mill is influential in determining the milling performance, with a mesh opening inclined to the direction of motion of the impeller leading to better gripping and minimising the production of fines. Yu et al. (2013) investigated the influence of magnesium stearate on formed ribbons of micro-crystalline cellulose (MCC) and di-calcium phosphate dihydrate (DCPD), and their subsequent milling performance in an oscillating mill. Comparing the MCC and DCPD ribbons, it was found that the size reduction in the mill could be related to the fracture energy measured by 3-point bend tests, although it should be noted that the DCPD ribbons were too fragile to be tested in this manner.

Hare et al. (2011) developed a method for predicting size reduction of pharmaceutical particles in an agitated vessel by estimating the bed stresses and strains using the Distinct Element Method (DEM). They related the experimentally-determined breakage to the applied stress and strain, the latter predicted by DEM. DEM is most commonly applied to spherical particles, though it can be used to represent non-spherical particles by the clumped sphere method (Favier et al., 1999). Moreno and Ghadiri (2003) simulated impact breakage of agglomerates generated using DEM with bonds of a given strength acting between contacting particles. The breakage mechanisms of chipping and fragmentation were both replicated by the DEM, with the extent of breakage being a function of the bond surface energy expressed by Weber number. Calvert et al. (2011) simulated aerodynamic dispersion of cohesive clusters by Computational Fluid Dynamics (CFD) coupled with DEM, and showed the same functional group is also applicable to their case. Breakage of non-spherical particles has also been investigated by Grof et al. (2011), who showed that DEM could be combined with experiments to develop breakage kernels for compression of needle-shaped particles. Kozhar et al. (2015) simulated the compression of irregular titania particles and demonstrated that the bonded sphere approach could better

capture the force-displacement response of the experiments, in comparison to the clumped sphere method.

To our knowledge DEM has not yet been applied to milling of dry compacted ribbons in the literature. Here we propose a combined experimental and computational approach to better understand the impact and shearing conditions that the ribbons experience under different mill operations, and to predict the resulting particle size distribution and residence time.

2. Materials and methods

The mill considered in this work is a rotary bar mill, as shown schematically in Fig. 1. It consists of a large horizontally-aligned hemi-cylinder with a length to diameter ratio of 1.89, and vertical side walls, within which four horizontal cylindrical bars of 20 mm diameter, held by a thin disc attached at each end, rotate around an axis, centrally aligned within the hemi-cylinder. The mill diameter is approximately 5–10 times the length of the ribbons. The cylinder is constructed using a sieve mesh with an outlet diameter of 3 mm, through which milled material exits. The rotating bars contact the hemi-cylinder when the mill is empty. However, as ribbons are fed into the top of the mill, the weight of feed material in the mill and the nipping of the ribbons by the rollers cause the sieve mesh to be separated from the bars by a narrow gap. As the ribbons enter the mill they may be impacted by a bar at the top of the mill, or they may bypass an upper bar and impact the base of the mill. The likelihood of impact at the top is influenced by the rotational speed of the bars, the sheet length and thickness, and entrance velocity. In the mill analysed here, the entrance velocity is determined by the vertical distance between the mill entrance and the roller compactor, and the feed rate to the roller compactor. Two ribbon formulations are considered in this work; formula A and formula B, as shown in Fig. 2. The ribbon lengths, widths and thicknesses are shown for both formulas in Table 1. After the fragments from initial impacts settle at the base of the mill they are continually sheared by the rotating bars until they are small enough to pass through the sieve mesh.

In this paper, a combined experimental and computational approach to predict milling performance of the above system is described (shown in Fig. 3), implemented and compared to plant data. To understand the impact velocities and stresses that the ribbons experience in the mill, the ribbons are represented in the DEM by using two separate approaches, namely clumped spheres, following the approach of Favier et al. (1999), and bonded spheres using the method developed by Brown et al. (2014). Since the
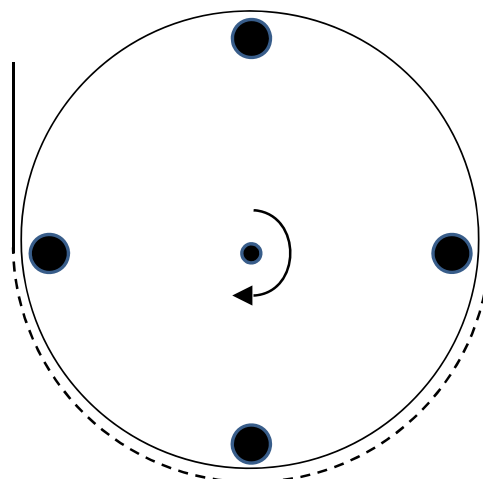
Fig. 1. Bar mill geometry.
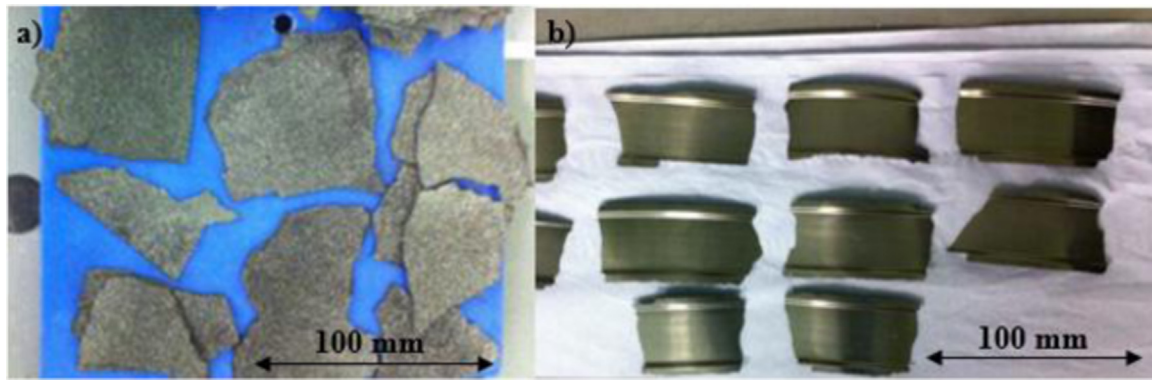
Fig. 2. Images of ribbons (a) formula A and (b) formula B.

Table 1
Ribbon dimensions for formulae A and B.

Formula	Length (mm)	Width (mm)	Thickness (mm)	Primary particle size, d_{50} (µm)	Shape
A	50–100	25–50	1.5–2.0	40	Flat
B	50–100	~25	0.8–1.0	3	Curved
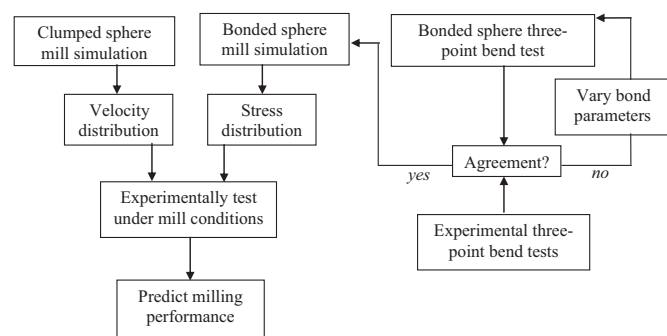
Fig. 3. Milling prediction approach.

clumped spheres remain rigidly attached for the duration of the simulation, regardless of forces experienced, this method is suitable for determining the initial impact conditions experienced by the ribbons by a bar at the top or the sieve mesh at the base. However, further information taken from such a simulation would not be representative of the true mill conditions, since the ribbons break significantly due to impact. Therefore, to analyse the stresses acting on the fragments, the latter method is used to represent the ribbons. This model ensures spheres remain rigidly aligned with other spheres to which they are bonded; however it allows bonds to be broken when they experience a stress greater than their strength. This approach would also be suitable for determining the initial impact velocities, however the clumped sphere approach is selected here to allow faster simulations to be obtained. For the bonded spheres, the bonds are characterised by the following properties: bond radius, Young's modulus, Poisson's ratio and compressive, tensile and shear strengths, and their distributions. A change in the values assigned to these parameters would lead to a different stress distribution in the mill and breakage pattern of the ribbons. Therefore, to ensure the ribbons are accurately represented by the bond parameters chosen, experimental three-point bend tests are carried out and simulated by the DEM. The bond parameters are varied in separate DEM simulations until the predicted breakage force is in agreement with the experimental data. The calibrated bond parameters are then used in the mill simulation to determine the dynamic conditions experienced by

the ribbons. Following the analysis of the impact velocity and shear conditions in the mill, the ribbons are exposed to these conditions in the experimental work to predict the particle size distribution of the mill product. To do this the ribbons are first dropped from a controlled height into a flat box with a rigid base, to ensure all fragments are retained. The drop height is varied to represent the distribution of impact velocities, as determined by the clumped sphere simulation. The impacted ribbon fragments are then collected and placed in a single layer in an annular shear cell (Ajax Equipment Ltd, Bolton, UK), based on the design of Paramanathan and Bridgwater (1983), compressed and sheared under the stresses and strains that were determined by the bonded sphere DEM mill simulations. The shearing process is carried out for all impacted material, which is then manually sieved using a 3.35 mm mesh sieve – to replicate the mill outlet. The shearing process is then repeated for all material that remains on the sieve, until the entire feed has passed through the sieve. Following this step the full size distribution is determined by a Retsch mechanical sieve shaker for 3 minutes at amplitude of 0.5 mm.

2.1. Clumped sphere mill simulation

The clumped sphere simulations were carried out using LIGGGHTS. The mill is represented by a solid hemi-cylinder with length to diameter ratio of 1.89, with flat ends and vertical side walls, with height equal to the hemi-cylinder radius, extending upwards above the horizontal diametric plane of the hemi-cylinder. Within the mill, four steel cylindrical bars of 20 mm diameter rotate around the horizontal axis of the mill, with their axes at a radial distance from the mill axis to provide zero clearance with the base of the mill, as shown in Fig. 4. The ribbons are represented by a single layer of contacting (but not overlapping) 1.8 mm diameter spheres, with a ribbon width of 25.2 mm (14 spheres) and lengths of 50.4 and 100.8 mm (28 and 56 spheres, respectively) in separate simulations. An example of the structure of the 50 mm ribbon is shown in Fig. 5. This approach is taken because the ribbons themselves are 1.8 mm thick. If the particle size were to be reduced to allow a double-layer of spheres in the ribbon, the number of spheres required would increase dramatically (by a factor of 8 if no sphere overlap were used), as would the computational time required. The properties of the wall and ribbon materials are provided in Table 2 and the interaction properties are provided in Table 3. The bars are rotated at 50 and 65 rpm in separate simulations, giving bar velocities of 0.92 and 1.19 m/s, respectively. Fifty vertically aligned sheets were individually generated immediately above the mill, with a generation interval of 1 sheet/s and an initial downward velocity of 2.5 m/s. The generation rate and velocity were determined from plant data of the feed rate of material into the roller compacter
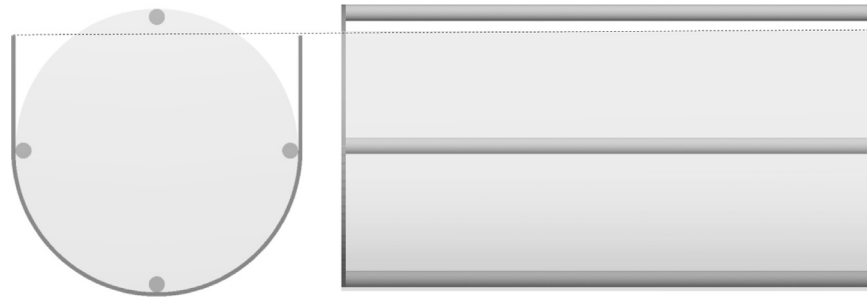
Fig. 4. Simulated mill geometry.
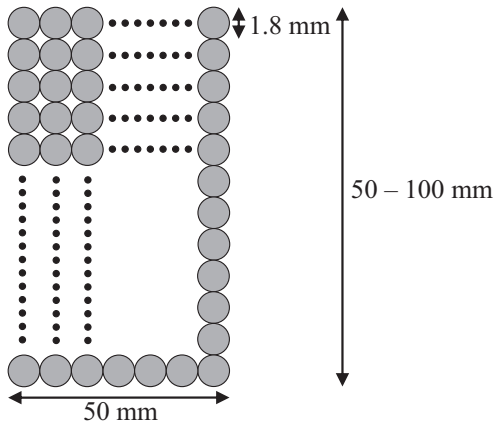
Fig. 5. Simulated ribbon using the clump sphere method.

Table 2
Simulation materials' properties.

Material Property	Ribbon	Mill (steel)
Density, ρ (kg/m^3)	4000 (A), 7000 (B)	7800
Shear modulus, G (GPa)	0.1	182
Poisson ratio, ν	0.25	0.25

Table 3
Simulation interaction properties.

Material Property	Ribbon–Ribbon	Ribbon-Mill (steel)
Coefficient of restitution	0.3	0.4
Coefficient of sliding friction (μ_s)	0.5	0.5
Coefficient of rolling friction, (μ_r)	0.01	0.01

(above the mill) and the vertical gap between the roller compactor and the mill entrance, assuming no deceleration due to air drag.

2.2. 3-Point bend experiments

A number of ribbons were evaluated by 3-point bend tests, in order for the process to be simulated by the DEM to determine representative bond strength parameters. The ribbons comprising formula A were of irregular shape, so they were cut to a length and width of 50 and 20 mm, respectively, prior to the test. The formula B ribbons were of regular width (26 mm), and hence were cut to a length of 50 mm prior to testing. In each test, a ribbon was placed on two supports with a gap of 25 mm, as shown in Fig. 6. A stainless steel beam, with a rectangular face and 0.5 mm thickness, was clamped above the ribbon (with its longest side aligned along the width of the ribbon) to a Stable Microsystems TA.XTplus Texture Analyser, fitted with a 500 g load cell. The beam was driven vertically downwards at a rate of 0.1 mm/s until the loaded
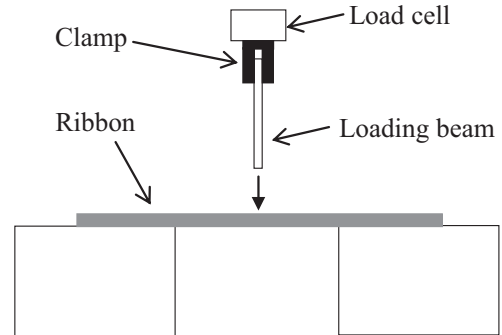
Fig. 6. Experimental 3-point bend test setup.

ribbon was broken, and the force displacement data recorded to determine the breakage force. Ten ribbons of each formulation were tested in this manner. The failure was essentially brittle with a sudden fall of load.

2.3. 3-Point bend test simulations

The 3-point bend tests were simulated in the DEM using EDEM software (DEM Solutions). The geometry setup was identical to that of the experimental procedure. In the model of Brown et al. (2014), used in these simulations, spheres are given a physical radius and a contact radius (the latter is greater than the former). If the *contact* radii of two spheres overlap then they are bonded at the time of bond creation. The ribbons were represented here in a similar manner to that outlined in Fig. 5, however the neighbouring spheres (with 0.9 and 0.45 mm radii for formulas A and B, respectively) were separated by a distance of 1 μm to enable generation of the square packing arrangement in EDEM. The contact radii had appropriate size to ensure horizontal neighbours were bonded but diagonal neighbours were not. The material properties of the mill and spheres are given in Table 2. The bond properties were varied (as discussed in Section 3.3) in separate simulations until the breakage force was within 10% of the experimental average, for each formula.

2.4. Bonded sphere mill simulation

The ribbons were created in the same manner as the 3-point bend test simulations, using the sphere and mill properties outlined in Table 2, and the optimum bond parameters from the simulated 3-point bend test. The mill setup was identical to that of the clumped sphere mill simulation, with the exception that the radial distance of the centre of the bars provides a gap of 1 mm between the bar and the hemi-cylinder mill. The ribbon length, formulation and mill speed were varied in separate simulations, as shown in Table 4. A total of eight ribbons were generated in each simulation. Since the contact model creates bonds between all contacting spheres (based on overlap of contact radii) at a

Table 4
Mill simulation conditions.

Test case	Formulation	Ribbon length (mm)	Mill speed (rpm)
1	A	50	50
2	A	50	65
3	A	100	50
4	A	100	65
5	B	50	50
6	B	50	65
7	B	100	50
8	B	100	65

Direction of box movement

Mill centre
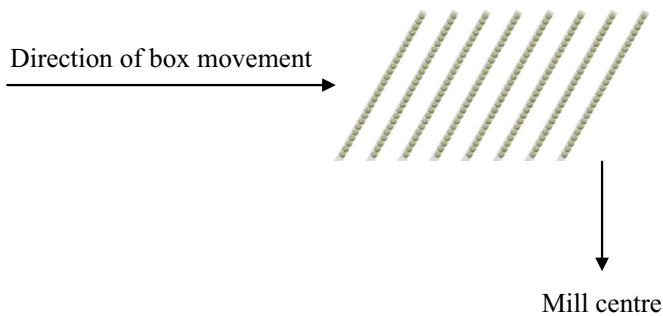
Fig. 7. Bonded sphere mill simulation.

specified timestep, the spheres for all ribbons were generated at the start of the simulation, with their velocity capped to zero until bonds had been created. Following bond creation, the velocity restriction was removed to allow the ribbons to fall under gravity. To ensure the ribbons entered separately, each was created within a bounding box, which was removed as needed to initiate the ribbon's fall. After each individual ribbon reached a vertical position entirely below the remaining ribbons, the next ribbon was moved horizontally across until it was in line with the centre of the mill. Once in this position, the box motion was stopped and the box was deleted to initiate the fall of the ribbon. The ribbons were inclined 30° to the vertical, since the ribbons tended to impact at approximately this angle in the experimental drop tests (described in Section 2.5). The simulation setup is shown in Fig. 7.

The stress, σ, acting on the ribbons, taken as normal, was determined from the force, F, acting on each individual bar in the mill, using Eq. (1). Since the bonded spheres represent flat sheets, the projected area, A_p, is approximated to equal the cross-sectional area of an individual sphere (taken as d_p^2, since the spheres have square packing arrangement) multiplied by the number of spheres in contact with the bar.

$$\sigma = \frac{F}{\sum_i^c A_p} \tag{1}$$

where c is the total number of sphere contacts with the given bar. The shear strain, Γ, for each pass of the roller was determined using Eq. (2).

$$\Gamma = \frac{V_r \cdot t}{d} \tag{2}$$

where V_r is the translational velocity of the bar, t is the duration of the shearing event (continuous period where $F > 0$) and d is the gap between the bar and the mill.

2.5. Ribbon impact experiments

The ribbons were vertically aligned and manually released from a height pre-determined to provide the corresponding vertical

impact velocity obtained from the clumped sphere mill simulations. The ribbons were dropped individually into a cubic Perspex container of length 250 mm, to retain all impacted fragments. The fragments were removed from the box before each subsequent test. The impact velocity was measured using a Redlake MotionPro X4 Highspeed Camera at 1000 frames/s. Ten ribbons were impacted for each mill condition simulated, and for each formulation. The fragments from all ribbons, impacted at conditions representing a single mill condition, were collected together and reserved for the shearing experiments. All ribbons rotated slightly as they were dropped, leading to impact angles of approximately 60° with the horizontal in all cases. This ribbon orientation was therefore introduced in the mill simulations. The impact angle would be highly influential on the extent of impact breakage, since at the two extremes the stress could propagate directly through the length or thickness of the ribbon, respectively.

2.6. Ribbon shearing experiments

The total mass of the fragments for a given ribbon formula was measured for those impacted at 2.75 m/s and those at 4 m/s. The product of the impact breakage experiments contained some material too large to be placed in the shear cell, i.e. its longest dimension being greater than 20 mm (the annular width of the shear cell). These large fragments were separated and their collective mass was measured. For formula A and B ribbons, 55 and 39% by mass, respectively was available for shear testing. The size distribution of milled products is not expected to be substantially affected by this, since successive milling events would break this material down sufficiently to allow its exit from the mill. However, a greater number of shearing events would be required to enable the material to exit from the mill.

The collected fragments were sheared in an Ajax attrition shear cell (Fig. 8), with inner and outer radii of 60 and 80 mm, respectively. Radial groove rings with a 2.5 mm pitch were fixed to the cell lid and base. The fragments resulting from the ribbon impact experiments were randomly selected to provide a single layer in the cell, onto which the cell lid was placed. The applied normal stress, σ, was varied by the addition of weights to the lid, to match that estimated by the bonded sphere mill simulation, as described by Eq. (3).

$$\sigma = \frac{F_l + F_w}{A_s} \tag{3}$$

where F_l and F_w are the gravitational force of the lid and weights, respectively, and A_s is the cross-sectional area of the shear cell annulus. The cell base was rotated whilst the lid rotation was prevented by a stopper arm, thus shearing the material in the cell. The angle of rotation, θ, was controlled to provide a shear strain equal to that estimated by the bonded sphere mill simulation, using Eq. (4).

$$\Gamma = \frac{\theta}{360} \frac{\pi \cdot D_c}{h} f \tag{4}$$

Cell lid

Gripping rings

Sample

Cell base
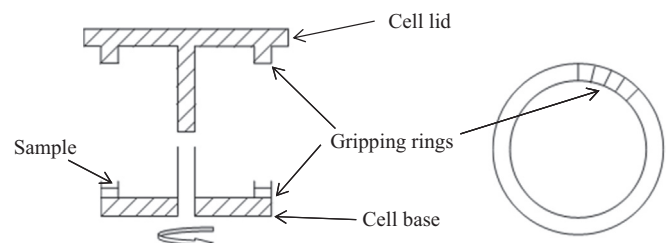
Fig. 8. Attrition shear cell.

where D_c is the median diameter of the cell (140 mm), h is the bed height (sheet thickness) and f is the grip factor, which was assumed to be 1.

After shearing all impacted fragments representing given mill operational conditions, the sheared material was manually sieved using a 3.35 mm mesh sieve – this being the closest available standard sieve to the 3 mm mesh outlet of the mill. Material passing through the sieve was reserved for final size analysis, whilst the material > 3.35 mm was sheared again under the same conditions, using the same bed preparation method outlined above. Once all the material passed through the 3.35 mm mesh sieve, its size distribution was collectively analysed. This material was placed on a stack of sieves with mesh sizes of 1000, 850, 600, 425 and 250 μm, and sieved using a Retsch AS 200 vibratory sieve shaker at an amplitude of 0.5 mm for 3 min. These sieving conditions were selected to ensure steady state and no breakage was observed during the sieving process.

Since each shearing event represents one pass of a mill bar against the outlet mesh, the residence time distribution is predicted from the fraction of material passing through the 3.35 mm sieve, x_{shear}, after shearing event N using (Eqs. (5) and 6).

$$x_{mill}\left(t_{res}\right) = \frac{m_{shear}}{m_{impact}} \sum_{1}^{N} x_{shear} \tag{5}$$

$$t_{res} = N\left(t_{shear} + t_{\text{int } erval}\right) \tag{6}$$

where $x_{mill}(t_{res})$ is the fraction of material having a residence time of t_{res} inside the mill, m_{shear} is the total mass of fragments sheared in the cell, m_{impact} is the total mass of fragments after the impact tests, and t_{shear} and $t_{interval}$ are the duration of a shearing event and interval between shearing events, respectively. Here, it is assumed that,

$$t_{\text{int } erval} = \frac{60}{\omega \cdot N_R} \tag{7}$$

where ω is the mill rotational speed (rpm) and N_R is the number of rollers in the mill (4).

3. Results and discussion

3.1. Clumped sphere simulation

The distribution of ribbon impacts at the top and bottom of the mill and the corresponding average impact velocities are shown in Figs. 9 and 10, respectively. Fig. 9 shows no clear influence of mill rotational speed or formulation on the percentage of impacts at
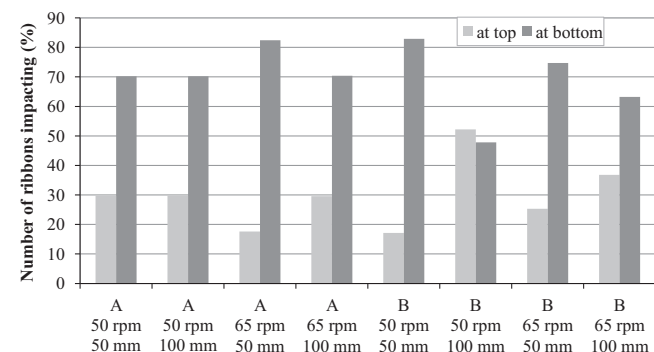
Fig. 9. Distribution of impacts of formulae A and B ribbons at the top and bottom of the mill.

the top and bottom of the mill, however there is an increased fraction of 100 mm ribbons impacting at the top of the mill, compared to the 50 mm sheets. This is to be expected since when the ribbon falls vertically the time that the ribbon spends in the vicinity of the bar at the top is greater for a longer ribbon, thus increasing the chance of being impacted by the bar. On average across the eight simulations about 30% of the ribbons impact at the top and 70% bypass the top bar and impact at the bottom.

Fig. 10 shows that in all eight cases the ribbons impacting the bottom have an average impact velocity of approximately 4 m/s. The ribbons impacting the top bar have a lower impact velocity, since they do not have as far to fall. Of the ribbons impacting at the top, those with a length of 100 mm exhibit a slightly lower impact velocity than those that are 50 mm in length. Overall the average impact velocity for the ribbons impacting at the top is 2.54 m/s.

3.2. Three-point bend test experiments

Representative force displacement curves for ribbons of formulas A and B are shown in Fig. 11. The formula A ribbons exhibit a sharp rise in force of approximately constant gradient until the breakage force is reached. In contrast the formula B ribbons show a gradually increasing force with displacement, which slows down until it drops quickly after the maximum force is reached. The trends were consistent across the ten samples tested of each formulae; differences may be caused by the variation in the mechanical properties of the ribbons, however the difference in their shape could also contribute towards this (see Fig. 2). The formula B ribbons have a radius of curvature of approximately 150 mm along their length, whereas the formula A ribbons are approximately flat. The formula B ribbons were loaded from the convex side in the 3-point bend tests. Visual observation indicates that failure occurs long before the maximum force is reached, however when broken the two fragments fall towards each other and provide further resistance to the driving beam before the two fragments fall downwards, and hence cause the behaviour observed in Fig. 11. Furthermore, loading of an arch delays failure, since the normal force is partially redirected laterally through the sample. Therefore this represents the maximum strength measured by this method, since if they were loaded from the concave side they would fail more easily. Nevertheless they are weaker than formula A ribbons.

The averages and distributions of the breakage force of formulae A and B ribbons are shown in Table 5. The average breakage force of formula A ribbons is more than double that of the formula B ribbons. For ribbons of each formula the coefficient of variation is comparable and of an acceptable range for the ten ribbons tested.

3.3. Three-point bend test simulation

Since the ribbons are very narrow, they are expected to break by snapping, which is caused by tensile and shear breakage. Therefore the bonds of the ribbons are expected to break in the simulations by exceeding their tensile or shear strength. The bond shear strength is manipulated in separate three-point bend simulations, along with the variation of bond strength and bond Young's modulus, whereas the compressive and tensile bond strengths are set to equal the shear strength. In all cases the Poisson ratio and bond radius multiplier were fixed at 0.25 and 1, respectively. The parameters used in separate simulations, along with the corresponding breakage forces, are shown in Table 6 and 7 for formulas A and B, respectively. A wide range of values were tested for Young's modulus and bond strength as the initial value selected did not yield a breakage force close to that of the experimental material. No direct relationship between the bond strength and Young's modulus to the breakage force was found.
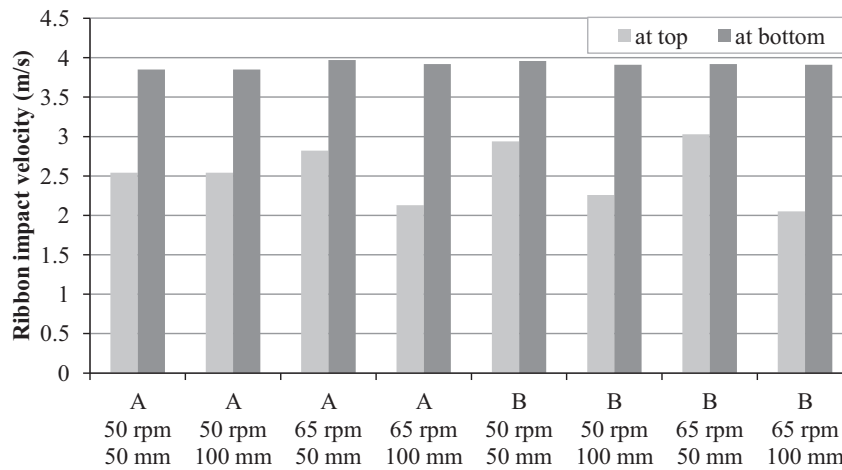
Fig. 10. Average ribbon impact velocities of formulae A and B ribbons at the top and bottom of the mill.
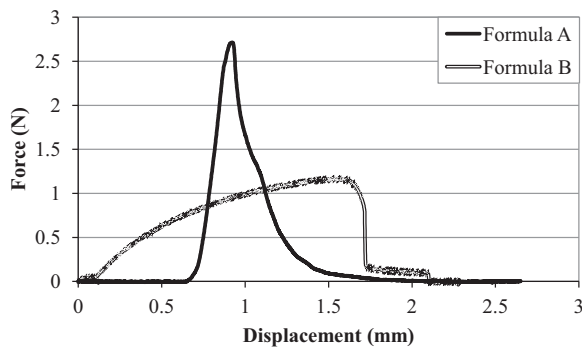
Fig. 11. Representative force displacement curves for ribbons of formulae A and B.

Table 5
Averages and distributions of ribbon breakage forces.

Measurement	Ribbon breakage force (N)	
Formula	A	B
Average	2.85	1.13
Minimum	1.73	0.62
Maximum	3.99	1.50
Standard deviation	0.69	0.25
Coeff. of variation	24.2%	21.7%

Table 6
Bond parameters for formula A ribbons.

Test case	Young's modulus (MPa)	Bond strength (MPa)	Ribbon breakage force (N)
1	0.2	0.032	0.07
2	2.0	0.032	0.04
3	2.0	0.2	0.01
4	2.0	1.25	0.14
5	2.0	2.0	0.26
6	4.0	0.2	0.22
7	8.0	0.2	0.20
8	8.0	0.4	0.43
9	60	2.9	2.98
10	60	4.0	3.93

For this reason the values were simply manipulated in an attempt to achieve the desired breakage force.

An increase in the bond strength results in an increased ribbon breakage strength (as expected), whereas an increase in bond Young's modulus leads to an increase in ribbon strength in some cases, but a decrease in ribbon strength in others. An infinite

Table 7
Bond parameters for formula B ribbons.

Test case	Young's modulus (MPa)	Bond strength (MPa)	Ribbon breakage force (N)
1	100	5	0.21
2	100	25	1.30
3	300	3.5	0.81
4	300	4.5	1.06
5	300	6	1.45
6	300	10	1.96
7	300	25	4.23

number of combinations of bond strength and Young's modulus able to reproduce the experimental breakage data should exist, however in this case we adopt a bond strength and Young's modulus of 2.9 and 60 MPa, respectively for formula A, and 4.5 and 300 MPa, respectively for formula B as they gave predictions closest to the experimental 3-point bend test results.

3.4. Mill simulation

The evolution of force, total contact area and stress on each bar of the mill for the simulation of formula A sheets, 50 mm in length under a mill speed of 50 rpm are shown in Figs. 12–14, respectively. Fig. 12 shows that the force on an individual bar rises rapidly from zero to a sharp peak, before reducing rapidly to zero, which approximately coincides with the force increase on the next bar. As would be expected, there is no obvious discrepancy between the forces acting on different bars. The peak force on the bars is initially steady, at approximately 5 N, but rises in an
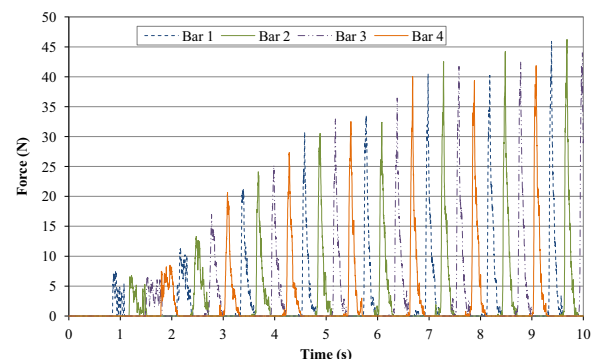
Fig. 12. Evolution of force on the bars at 50 rpm for formula A sheets 50 mm in length.
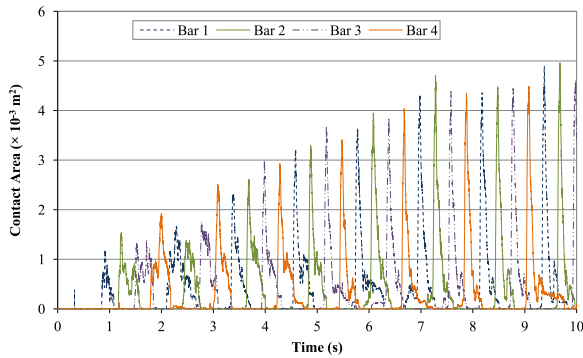
Fig. 13. Evolution of total contact area on the bars at 50 rpm for formula A sheets 50 mm in length.
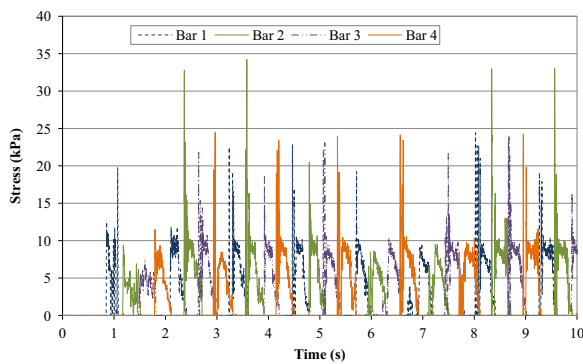
Fig. 14. Evolution of stress on the bars at 50 rpm for formula A sheets 50 mm in length.

approximately linear fashion after 2 s of simulation time. The rise in force appears to be due to the ribbons breaking up into smaller fragments and hence creating a greater area contacting the bars, as shown in Fig. 13, since the trend matches the force trend remarkably well. Consequently the average peak stresses, calculated by Eq. (1), remain relatively unchanged throughout the simulation, as shown in Fig. 14.

The maximum stress of each shearing event (continuous period of greater than zero force on a given bar) is determined, and the average maximum stress of all shearing events is considered to provide a characteristic stress of the mill under a given operation condition. These stresses are shown in Table 8, along with the average duration of each shearing event, t, and the corresponding strain, Γ, calculated using Eq. (2), where V_r is the radial distance of the centre point of a bar multiplied by the rotational speed. For the formula A ribbons there is minimal effect of sheet length and rotational speed on the prevailing stresses; however an increase in rotational speed causes a decrease in the average stress duration, and consequently the shear strain. This may be due to the ribbon

Table 8
Characteristic normal stresses and shear strains in the mill for formulae A & B ribbons.

Formula	A	A	A	A	B	B	B	B
Mill speed (rpm)	50	50	65	65	50	50	65	65
Sheet length (50 mm)	50	100	50	100	50	100	50	100
Max stress (kPa)	26.8	26.7	27.3	29.6	0.6	1.4	1.2	1.6
Average stress (kPa)	5.2	5.3	6.4	6.1	0.000	0.036	0.036	0.032
Average stress duration, t_{shear} (s)	0.19	0.22	0.08	0.1	0.05	0.03	0.03	0.02
Strain (−)	168	250	93	116	43	26	29	22
Angle of shear cell rotation (°)	124	184	68	85	–	–	–	–

fragments being moved away from the shearing zone more rapidly at 65 rpm than 50 rpm. The prevailing stresses and strains are significantly lower for the formula B ribbons. This is due to these ribbons being slightly narrower than the clearance (0.9 mm compared to 1 mm), hence these results are not expected to be representative of the real milling conditions for formula B ribbons. Consequently the prevailing conditions of stress and strain predicted for formula A ribbons are also applied to formula B ribbons in the shear cell.

3.5. Ribbon impact experiments

As shown in Figs. 9 and 10, the impact velocity distribution showed little variation with the milling parameters, hence the same conditions were used for impacts representing each mill condition and formula. Forty ribbons were randomly selected for each formula, ten of these (25%) were subjected to impacts at 2.75 m/s (representing impacts at the top) and thirty (75%) were subjected to impacts at 4 m/s (representing impacts at the bottom). Drop heights of 60 and 100 mm were found to provide impact velocities of 2.75 and 4 m/s, respectively. Visual observation indicated that the formula B ribbons were more prone to breakage, and the extent of breakage increased significantly when the impact velocity was increased from 2.75 to 4 m/s. Fig. 15 shows images immediately after impact of both ribbon formulas at the two velocities.

3.6. Ribbon shearing experiments

The ribbons of formulae A and B were tested independently. In each case the mass of fragments remaining from each impact velocity was divided equally into four samples for testing under both mill speeds and for both sheet length conditions. For a given mill condition the sample material comprised of the combined fragments from the 2.75 and 4 m/s impacts. The ribbon shearing experiments were carried out as described in Section 2.6, using the maximum stress and strain conditions shown in Table 8. Since the stress and strain conditions in the mill for the formula B ribbons were deemed to be unrealistically low, these ribbons were tested using the same conditions as those estimated by the DEM for the formula A ribbons. The fraction of the fragments passing through the 3.35 mm sieve after each shearing event is shown in Table 9 for each mill condition for the two ribbon formulas. All fragments of formula A ribbons pass through the sieve, and are therefore predicted to exit the mill after three to six shearing events. Fewer shearing events are required to reduce all fragments to a sieve size < 3.35 mm with sheet lengths of 100 mm in comparison to 50 mm. This is expected to be largely caused by the increased strain for these conditions (see Table 8), since the maximum stresses are relatively similar.

The size distributions of all material which has passed through the 3.35 mm sieve for the different mill conditions are shown in Figs. 16 and 17, for formulas A and B, respectively. The predictions of milling performance for formula A ribbons are compared to plant milling data of these ribbons in the described mill in Fig. 16. The predictions suggest that in all tested milling conditions, more than half of the material is greater than 1 mm (sieve mid-point 2175 μm corresponds with 1 – 3.35 mm), with a significant amount of fines (< 250 μm) being generated. These predictions match the plant data reasonably well. The difference amongst the predicted size distributions for different milling conditions is small; the greatest difference being that at 65 rpm with ribbons of 50 mm the fraction of material greater than 1 mm is notably greater and there are fewer fines compared to the other cases. This difference is expected to arise due to the lower strain applied in the shear cell experiments for 65 rpm with ribbons of 50 mm. This
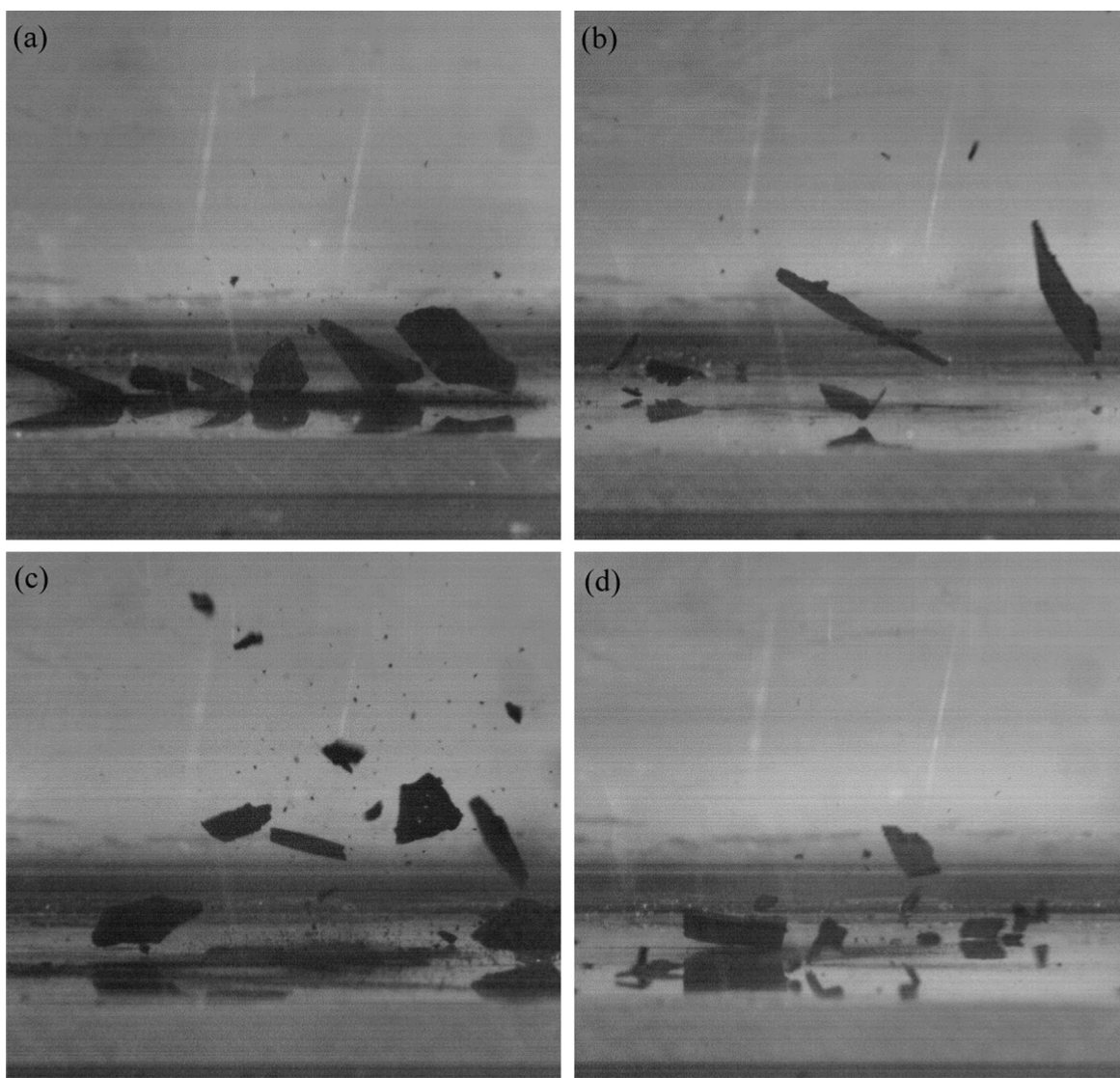
Fig. 15. Ribbons immediately after imact (a) formula A at 2.75 m/s, (b) formula B at 2.75 m/s, (c) formula A at 4 m/s, (d) formula B at 4 m/s.

Table 9
Mass of fragments passing through 3.35 mm sieve after each shearing event.

Formulation	A	A	A	A	B	B	B	B
Mill speed (rpm)	50	50	65	65	50	50	65	65
Sheet length (mm)	50	100	50	100	50	100	50	100
Number of events, N	Fragment mass fraction, m_d/m_s (%)							
1	42	51	37	48	94	94	82	77
2	67	68	54	77	100	100	100	100
3	84	87	68	92	100	100	100	100
4	97	100	85	100	100	100	100	100
5	100	100	96	100	100	100	100	100
6	100	100	100	100	100	100	100	100

Fig. 16. Predicted and plant particle size distributions of formula A ribbons.

milling condition gives the closest prediction to the plant data, although overestimates the amount of fines. A number of assumptions are involved in the prediction approach taken here, such as the assumption that all ribbon fragments lay flat in the mill before being sheared, and the assumption that the surface of the shear cell is similar to that of the bars and mill mesh. The teeth of the shear cell gripping rings could lead to wear across the ribbon surface that does not occur in the mill, thus generating a greater quantity of fines. Further to this, the shear cell tests used in the prediction approach ensure all material is sheared for the full duration of the shearing event, thus small fragments may be

broken further, whereas in the mill fine particles will percolate through the fragments and exit the mill. These factors would contribute to the overestimate of fine particle generation.

The milling predictions of the formula B ribbons are shown in Fig. 17. As with the formula A ribbons, the majority of the mill products are either > 1 mm or < 250 µm. However, there is a much greater change in size distribution with the milling conditions, with the fraction > 1 mm varying from 16 to 54%. The greatest extent of breakage (more material < 600 µm) occurs for 50 rpm and 100 mm, followed by 50 rpm and 50 mm, 65 rpm and
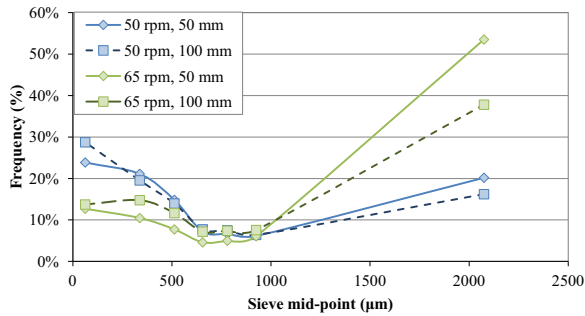
Fig. 17. Predicted size distributions of formula B ribbons.
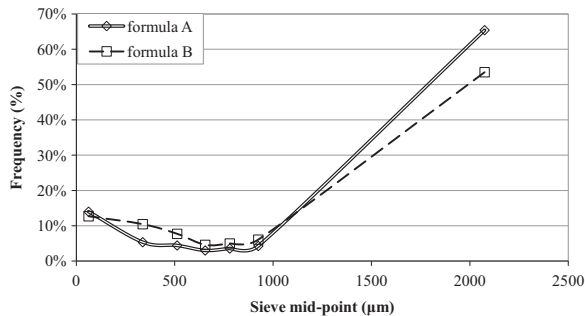
Fig. 18. Comparison of predicted size distributions of the two ribbon formulas milled at 65 rpm with ribbon lengths of 50 mm.

100 mm, and finally 65 rpm and 50 mm. When comparing to the conditions applied in the shear cell experiments (Table 8), this corresponds to an increase in strain causing an increase in breakage. The fraction of product in the 600 µm to 1 mm size range is predicted to be relatively unchanged by the milling conditions.

Fig. 18 shows the predicted size distributions of formula A and B ribbons with length 50 mm milled at 65 rpm. The quantity of fines (< 250 µm) is predicted to be similar for ribbons of both formulas, however formula B is predicted to have a greater amount of material 250–600 µm, and a smaller fraction > 1 mm, suggesting that formula B ribbons break more extensively in the mill. This is expected based on the 3-point bend test measurements (Table 5 and Fig. 11).

The residence time of formula A material passing through the 3.35 mm sieve after N shearing events is estimated using (Eqs. (5), 6) and (7), and is shown in Fig. 19. The residence time distribution is strikingly similar for all conditions except for ribbons of 100 mm in length and a mill speed of 65 rpm, where the material is predicted to exit the mill quicker. This discrepancy is caused by both the small number of shearing events required to ensure all fragments pass through the 3.35 mm sieve, and the shorter t_{shear} predicted by the DEM mill simulations at 65 rpm. It should be
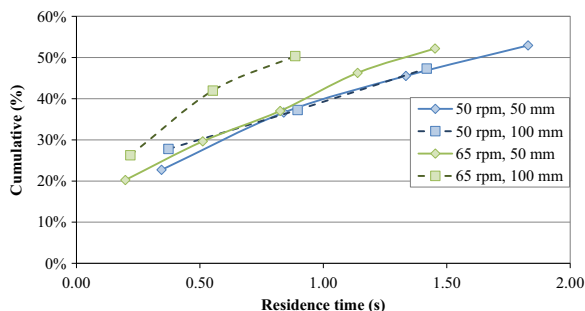
noted that the fragments that are too large to be sheared in the shear cell would be expected to generate some material small enough to exit the mill after each shearing event, as such the residence time distribution shown in Fig. 19 represents an underestimate of the amount of material exiting the mill after a given time.

In this work, limited material was available, thus allowing only a narrow range of milling conditions to be investigated. If sufficient material were available, a wider range of stresses and strains could be applied in separate tests to determine their individual influences on the resulting breakage. Such testing would allow an empirical breakage relationship to be developed using the Neil and Bridgwater (1994) method, which when coupled directly with the evolution of stress during shearing events (e.g. Fig. 14), in a similar manner to that of Hare et al. (2011), would give a more accurate prediction of the milling performance. This would also allow modelling under different mill conditions to be carried out and the milling performance predicted without further experimental work.

4. Conclusions

A method for predicting the size reduction of dry compacted ribbons in a rotary bar mill has been described and implemented for two ribbon formulas. The method utilises a bonded sphere DEM model to represent the ribbons, with the bond properties determined by three-point bend test simulations compared to experiments. The DEM of the mill is used to predict the impact velocities and peak stresses and strains that the ribbons, and their fragments, experience. Ribbons are then subjected to impact events by dropping them from a controlled height, and then the fragments are sheared in a shear cell under the conditions predicted from the DEM. Fragments that do not pass through a sieve, representing the outlet mesh size of the mill, are sheared again until all material passes through this sieve. A full size analysis then provides a prediction of the product size distribution of the mill. The method is applied here for mill speeds of 50 and 65 rpm, and ribbon feed lengths of 50 and 100 mm. It is predicted that these conditions do not significantly alter the product size distribution. There is a good agreement between the prediction and plant data of ribbon formula A. Formula B ribbons are predicted to break more easily than formula A ribbons in the mill, which correlates with the three-point bend measurements and qualitative analysis of the impact breakage.

If a greater amount of material is available for shear cell testing, the above method could be extended to develop a relationship of particle size to stress and strain. Such a relationship could be applied to the full profile of the evolution of stress and strain in the mill, and thus lead to a more robust prediction method. In addition it would be beneficial to understand the relationship between the mass of material in the mill and the deflection of the mill mesh, and ultimately the influence of roller-mill clearance on stress and strain.

Fig. 19. Predicted mill residence time for formula A.

Appendix A. Supplementary material

Supplementary data associated with this article can be found in the online version at http://dx.doi.org/10.1016/j.ces.2016.04.041.

References

Al-Asady, R.B., Osbourne, J.D., Hounslow, M.J., Salman, A.D., 2015. Roller compactor: the effect of mechanical properties of primary particles. Int. J. Pharm. 496, 124–136.

Brown, N.J., Chen, J.-F., Ooi, J.Y., 2014. A bond model for DEM simulation of cementitious materials and deformable structures. Granul. Matter 16 (3), 299–311.

Calvert, G., Hassanpour, A., Ghadiri, M., 2011. Mechanistic analysis and computer simulation of the aerodynamic dispersion of loose aggregates. Chem. Eng. Res. Des. 89 (5), 519–525.

Favier, J.F., Abbaspour-Fard, M.H., Kremmer, M., Raji, A.O., 1999. Shape representation of axi-symmetrical arbitrary particles in discrete element simulation using multi-element model particles. Eng. Commun. 16, 467–480.

Grof, Z., Schoellhammer, C.M., Rajniak, P., Štěpánek, F., 2011. Computational and experimental investigation of needle-shaped crystal breakage. Int. J. Pharm. 407, 12–20.

Guigon, P., Simon, O., Saleh, K., Bindhumadhaven, G., Adams, M.J., Seville, J., 2007. Roll pressing. In: Salman, A.D., Hounslow, M., Seville, J.P.K. (Eds.), Granulation. Elsevier, Amsterdam, pp. 255–288.

Hare, C., Ghadiri, M., Dennehy, R., 2011. Prediction of attrition in agitated particle beds. Chem. Eng. Sci. 66, 4757–4770.

Khorasani, M., Amigo, J.M., Sonnergaard, J., Olsen, P., Bertelsen, P., Rantanen, J., 2015. Visualization and prediction of porosity in roller compacted ribbons with near-infrared chemical imagin (NIR-CI). J. Pharm. Biomed. Anal. 109, 11–17.

Kozhar, S., Dosta, M., Antonyuk, S., Heinrich, S., Bröckel, U., 2015. DEM simulations of amorphous irregular shaped micrometer-sized titania agglomerates at compression. Adv. Powder Technol. 26, 767–777.

Miguelez-Moran, A.M., Wu, C.-Y., Seville, J.P.K., 2008. The effect of lubrication on density distributions of roller compacted ribbons. Int. J. Pharm. 362, 52–59.

Moreno, R., Ghadiri, M., 2003. Effect of impact angle on the breakage of agglomerates: a numerical study using DEM. Powder Technol. 130, 132–137.

Muliadi, A.R., Litster, J.D., Wassgren, C.R., 2013. Validation of 3-D finite element analysis for predicting the density distribution of roll compacted pharmaceutical powder. Powder Technol. 237, 386–399.

Neil, A.U., Bridgwater, J., 1994. Attrition of particulate solids under shear. Powder Technol. 80, 207–219.

Paramanathan, B.K., Bridgwater, J., 1983. Attrition of solids – I: cell development. Chem. Eng. Sci. 38 (2), 197–206.

Salman, A., Hounslow, M., Seville, J.P.K., 2007. Granulation, First ed. Elsevier, Amsterdam.

Samata, A.K., Ng, K.Y., Heng, P.W.S., 2012. Cone milling of compacted flakes: process parameter selection by adopting the minimal fines approach. Int. J. Pharm. 422, 17–23.

Vanarase, A., Aslam, R., Oka, S., Muzzio, F., 2015. Effects of mill design and process parameters in milling dry extrudates. Powder Technol. 278, 84–93.

Yu, S., Adams, M., Gururajan, B., Reynolds, G., Roberts, R., Wu, C.-Y., 2013. The effects of lubrication on roll compaction, ribbon milling and tabletting. Chem. Eng. Sci. 86, 9–18.